

Space charge effects in ultrafast electron diffraction and imaging

Zhensheng Tao, He Zhang, P. M. Duxbury, Martin Berz, and Chong-Yu Ruan^{a)}

Physics and Astronomy Department, Michigan State University, East Lansing, Michigan 48824-2320, USA

(Received 14 November 2011; presented 20 December 2011; published online 24 February 2012)

Understanding space charge effects is central for the development of high-brightness ultrafast electron diffraction and microscopy techniques for imaging material transformation with atomic scale detail at the fs to ps timescales. We present methods and results for direct ultrafast photoelectron beam characterization employing a shadow projection imaging technique to investigate the generation of ultrafast, non-uniform, intense photoelectron pulses in a dc photo-gun geometry. Combined with N-particle simulations and an analytical Gaussian model, we elucidate three essential space-charge-led features: the pulse lengthening following a power-law scaling, the broadening of the initial energy distribution, and the virtual cathode threshold. The impacts of these space charge effects on the performance of the next generation high-brightness ultrafast electron diffraction and imaging systems are evaluated. © 2012 American Institute of Physics. [doi:10.1063/1.3685747]

I. INTRODUCTION

Electron microscopy and diffraction are the most widely used and essential tools for determining the structure and composition of matter at the nanometer scale. Currently, space charge effects are the key limiting factor in the development of ultrafast atomic resolution electron imaging and diffraction technologies,¹⁻⁴ which would enable imaging of ultrafast electronic and chemical processes at the single site level.⁵⁻⁸ The debate over whether high brightness can co-exist with high temporal and spatial resolution lies in the recompression of longitudinal electron pulse-length to their initial values, limited only by photoemission processes prior to the space-charge-led smearing of phase space. Two pressing issues to be elucidated are the space-charge limit of high flux photoemission, which leads to broadening of the initial phase space⁹ and the Coulomb explosion during propagation in free space.¹⁻³ In recent development of MeV RF guns triggered by fs laser pulses, a high ac extraction field is employed to allow the generation of extremely high brightness and short duration-pulsed electron beams for accelerator applications,¹⁰ benefiting from the relativistic time dilation to suppress the Coulomb explosion. However, the high energy beams produced from ac guns are deleterious to nanoscale material studies and are subject to poor beam and image quality, due to small scattering angles and limitations in electron lenses. The pathway to the next generation of ultrafast imaging and diffraction technologies is the use of dc guns with relatively low energies (≤ 1 MeV). The experimental ability to image the spreading of fs electron pulses enables precise experimental characterization of space charge effects and the systematic design of technologies¹¹⁻¹⁸ to overcome space charge effects that limit current high flux ultrafast dc gun development. In this paper, we extend a novel ultrafast electron shadow projection imaging technique¹⁹ to interrogate space charge effects shortly after photoemission and during free space expansion. We present essential scaling features associated with the fs high density

nonequilibrium beam dynamics resulting from space charge effects and determine the virtual cathode limit of fs intense photoemission and the initial pulse characteristics required to quantitatively model the intense photoelectron pulses in a high brightness photoelectron beam column. We evaluate the performance of the next generation ultrafast electron diffraction and imaging systems incorporated with an RF compressor to remediate the free-space space-charge effect (Coulomb explosion). The limits on the combined spatial (probe size) and temporal resolution in different operational regimes are discussed.

II. MEASUREMENT OF SPATIAL AND TEMPORAL EVOLUTION OF PHOTO-ELECTRON PULSES

The photoelectron pulse dynamics can be directly investigated by a shadow projection imaging technique,¹⁹ which monitors both the transverse and longitudinal electron pulse profiles at the ultrafast time scale. Here, we investigate the photoelectron pulse dynamics in a dc photo-gun arrangement employing a gold photocathode triggered by UV fs laser pulses [50 fs, photon energy $\hbar\omega(\lambda = 266 \text{ nm}) = 4.66 \text{ eV}$] at high intensities (10^5 – 10^8 electrons per pulse), relevant for high brightness implementations of ultrafast electron diffraction^{1,3,7,20} and imaging.^{21,22} The photocathode (gold film) is prepared via vapor deposition on a quartz substrate with a homogeneous film thickness of 30 nm. The photon energy is slightly higher than the reported work function (Φ_w) of gold film that ranges from 4.0–4.6 eV,²³⁻²⁶ allowing photoemission with a small energy spread. The shadow projection imaging technique is utilized to investigate the space charge effects in the generation of fs electron pulses in a geometry depicted in Fig. 1(a), where a positive electrode (anode) is separated 5 mm from the cathode, providing an applied field (F_a) to facilitate photoemission. The fs laser pulses arrive at the cathode surface at 45° incidence and define the zero-of-time for photoemission. The dynamics of the surface-emitted electron pulse is imaged through the projection of a point electron source (P) that casts a shadow from the electron pulse onto a metalized phosphor screen connected to an

^{a)}Electronic mail: ruan@pa.msu.edu.

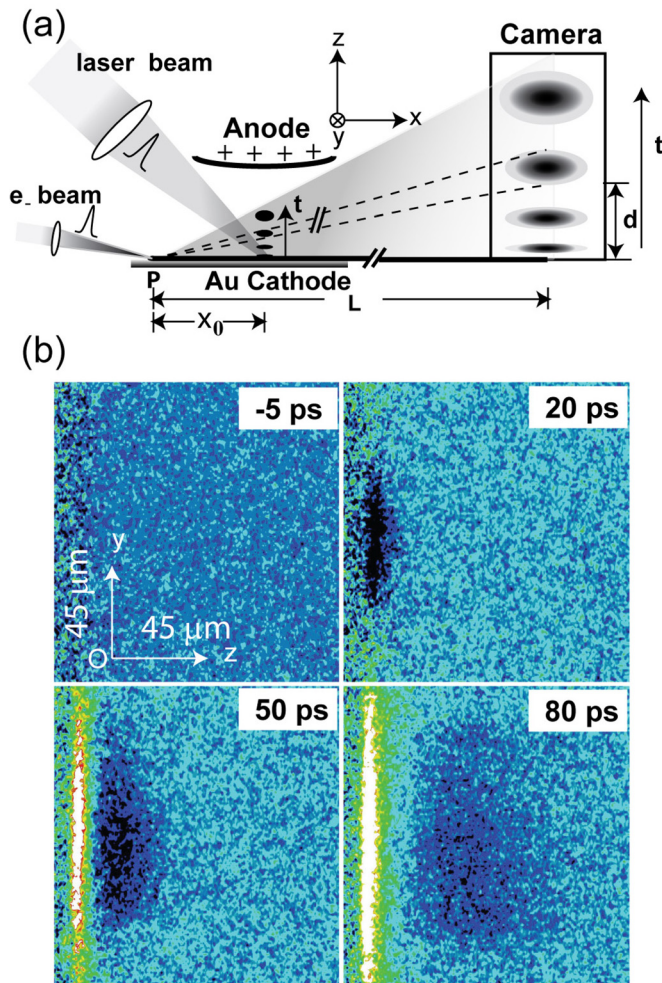


FIG. 1. (Color online) Electron point-projection imaging technique and results. (a) Schematic of the experiment. For illustration purposes, the angular span of the shadow is significantly increased from typical values ≤ 1 mrad. For this reason, the projection is nearly linear. (b) The snap-shots of the normalized shadow images at selected times. The magnification of the projection imaging is ≈ 33 .

intensified CCD camera. The point electron source is generated by focusing an independent low density fs photoelectron beam²⁷ containing ≈ 800 e/pulse with a beam waist of 5–10 μm ,²⁷ which is synchronized to the exciting laser beam with a well-defined delay (Δt) controlled by an optical delay stage (Newport: 2MS6WCC) capable of clocking the probing electron beam with respect to photoemission at ≤ 10 fs precision.

The projection imaging is performed at 1 kHz for each delay, and snap-shot images at each delay Δt are averaged over 10^5 – 10^6 repetition pump-probe cycles to obtain sufficient signal-to-noise ratio and to average out the pulse-to-pulse fluctuations of pump and probe pulses. The shadow patterns, obtained by taking the difference between the positive frames ($\Delta t > 0$) and the negative frame ($\Delta t < 0$), are normalized to the negative frame image to cancel out the angular dependence of the illumination from the point source.

Quantitative results are obtained through fitting the experimental data with an analytical expression describing the projection geometry.¹⁹ For example, a linescan over the shadow profile (Fig. 1(b)) along z has a form

$$F(d) = \frac{B \Sigma}{\sigma_z} \frac{\text{Exp} \left[-\frac{(dx_0 - Lz_0)^2}{2(d^2\sigma_x^2 + L^2\sigma_z^2)} \right]}{\sqrt{\frac{1}{\sigma_x^2} + \frac{d^2}{L^2\sigma_z^2}}}, \quad (1)$$

where d is the position on the camera screen, Σ is the electron charge density, x_0 is the source-to-beam distance, z_0 is the electron pulse's center of mass (COM) position, σ_x and σ_z are the widths in transverse and longitudinal directions, and L is the camera distance. Similar form along y direction can be obtained by replacing σ_z with σ_y and removing z_0 term in Eq. (1). The key pulse parameters, such as Σ , z_0 , σ_z , and σ_y can be determined by fitting its longitudinal and transverse shadow profiles, which evolve as a function of time. The quantitative aspect of shadow imaging technique has been verified with an N-particle shadow projection imaging simulation—see Fig. 8 and relevant discussions in Ref. 28. In this specific experiment, $x_0 = 5.0$ mm and $L = 16.5$ cm, giving a magnification $M \approx 33$ for imaging. While Eq. (1) considers nonlinearity in the projection imaging, the projection is in the linear regime when $\sigma_y, \sigma_z \ll L, d$. In our front illumination geometry, the exciting laser has an elliptical footprint with $\sigma_x = 115$ μm and $\sigma_y = 81$ μm , determined *in situ* via examining surface voltammetry characterization.^{19,28} Characterization of the laser footprint on the photocathode yields an initial transverse profile of the photo-emitted electrons consistent with the transverse electron bunch characterization from shadow imaging. Laser footprint characterization also yields quantitative measurements of the laser fluence (F) and, combined with Σ obtained from imaging, the number of emitted electrons (N_e). Imaging experiments are performed using various exciting fluences $F = 1$ –10 mJ/cm^2 and extraction $F_a = 0$ –0.4 MV/m, which together produce a wide range of values of N_e up to 10^8 electrons/pulse.

Direct visualization of the Coulomb explosion of electron pulses is achieved by the shadow imaging, as shown in Fig. 1(b). To quantify the rate of Coulomb explosion, the time-dependent CoM frame electron pulse length $\sigma_z(t)$ is extracted from the shadow profile as a function of electron density. Since, here, the electron longitudinal profile is observed to expand rapidly while the transverse profile increases little ($\leq 15\%$) over our tracked time window (0–120 ps), electron sheet density Σ , defined as $\Sigma = N_e/(\pi\sigma_x\sigma_y)$, is a more appropriate parameter than N_e for characterizing the space charge effects. We extract from the shadow imaging data the dependence of the electron pulse-length on Σ . Figure 2(a) shows a superlinear increase of $\sigma_z(t)$ resulting from the strong space charge effects at high sheet density Σ , whereas at low Σ , $\sigma_z(t)$ changes linearly with a slope approaching 0.1 $\mu\text{m}/\text{ps}$, which translates to a very small longitudinal photoelectron energy spread of 0.03 eV, supporting the over-the-barrier direct photo-ionization picture. As will be discussed later, in the weak emission limit, the initial momentum spread of the photoelectron pulse compares well with the theory of the three-step model designed to model the photoemission at the single-electron (space charge-free) limit.^{30,31} At high Σ , we observe an increase of the initial time derivative of $\sigma_z(t)$, suggesting a perturbation of the initial phase space by intense photoemission.

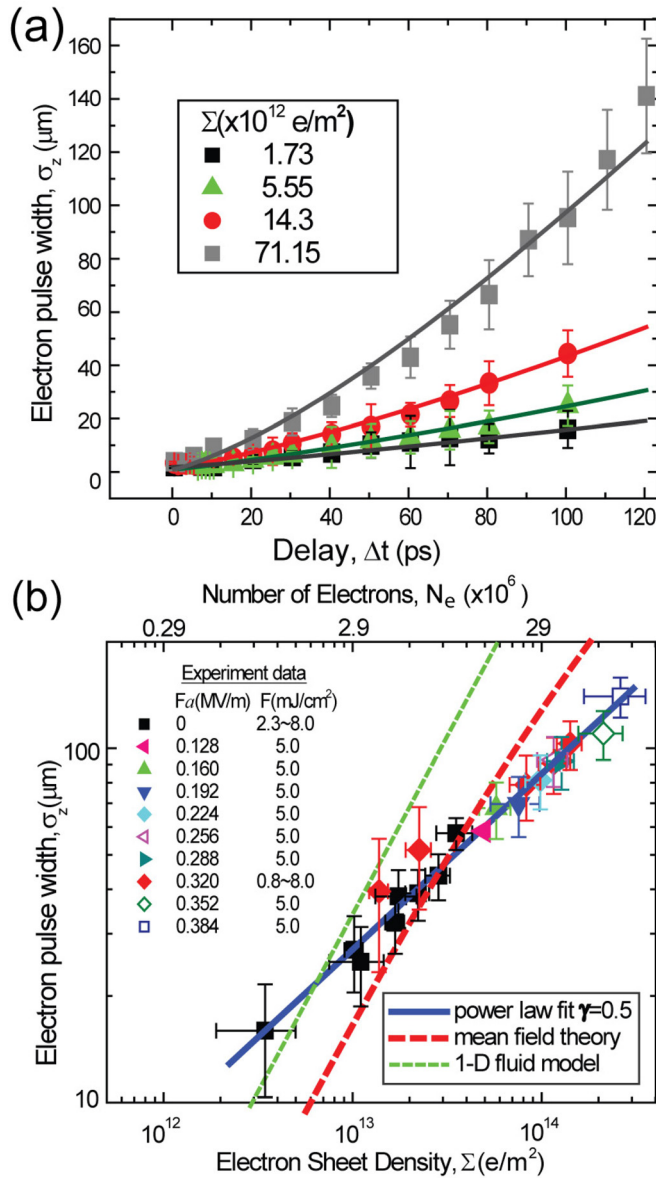


FIG. 2. (Color online) The results of electron point-projection imaging. (a) The CoM frame expansion dynamics of electron pulses with longitudinal pulse length σ_z . The solid lines through the experimental data (symbols) are from N-particle simulations. (b) Dependence of pulse length on the electron sheet density at time 100 ps for various F and F_a settings, showing a universal power-law increase with exponent roughly $\gamma = 0.5$. Predictions based on mean-field (Ref. 3) and one-dimensional (1D) fluid (Ref. 29) models are also presented.

III. THE SPACE CHARGE EFFECTS AND MODELING

To elucidate the space charge effects in the observed photoelectron dynamics, we employ N-particle dynamics simulations to model the experimental results. In particular, we investigate how pulse spreading depends on electron density and the initial conditions required to reproduce the pulse spreading trajectories using N-particle simulations.

A. Fractional power-law dependence in the space-charge-led pulse lengthening

First, we investigate the scaling of the pulse spreading with respect to the electron density Σ . We extract the longi-

tudinal pulse-length (σ_z) at 100 ps from data sets using different extraction field (F_a) or fluence (F) and plot σ_z as a function of Σ . Interestingly, we observe a power-law scaling of σ_z with Σ with an exponent that is significantly smaller than one, irrespective of the applied extraction field (F_a) or fluence (F), as presented in Fig. 2(b). Our results differ from the energy-dependent space-charge-led pulse lengthening measurements based on streaking technique, which determines σ_z at a fixed probe location.¹ Since ultrafast imaging tracks temporal development of σ_z in the CoM frame, this explains why there is no explicit energy (or F_a) dependence in our data. Furthermore, since, according to Fig. 2(b), a high Σ can be achieved with either high F_a or F , the observation of CoM $\sigma_z(t)$ being exclusively parameterized by Σ indicates the origin of the power-law scaling is mainly due to space charge effects. Here, σ_z is obtained at 100 ps, and to a very good approximation, the power-law exponent γ is near 0.5. At earlier times, γ is smaller, as depicted in the inset of Fig. 3(a). For example, at 40 ps, $\gamma \approx 0.37$, and at 60 ps, $\gamma \approx 0.43$, while for later times, γ increases slowly. We identify that this time-dependent scaling behavior with a terminal γ varying between 0.5 and 1 is a manifestation of a nonuniform photoelectron pulse profile seeded with different initial conditions. The dynamics of a uniform charge distribution can be analytically described by envelope-based approaches, such as mean-field,³ fluid,²⁹ or self-similar³² space charge models. When the charge distribution is non-uniform, the pulse length was estimated by the mean-field theory with a scaling factor.^{3,32} However, the temporal evolution of the pulse length scales differently depending on the shape of the pulse.³² This is best described with the transient power-law growth as a function of Σ . The uniform charge density evolves self-similarly with $\gamma \approx 1$, as shown in Fig. 2(b). We show that the longitudinal pulse profile remains largely near-Gaussian up to 120 ps (Fig. 3(b)), and the growth exponent γ is less than 1. We expect that, at long times, the effect of internal space charge forces decreases and the lateral expansion is important, leading γ to saturate between 0.5 and 1, as indicated in Fig. 3(a).

B. Density-dependent broadening of initial electron velocity distribution

When there is a significant initial momentum spread (Δp), the evolution of the electron pulse length $\sigma_z(t)$ at the shortest time is linear with a slope equal to $\Delta p/m_e$.¹⁹ The distinctive $\sigma_z(t)$ from several different Σ s, reported by $\sigma_z(t)$ in Fig. 2(a), serve as the bases to investigate the near cathode space charge effect by fitting them with N-particle simulations. To parameterize the shape of the phase space, we define a chirp parameter a in the N-particle simulations. When $a = 0$, the electron pulse is fully thermal with no correlation between momentum and position, while, in the $a = 1$ limit, there is a perfect correlation between the position and momentum, as described in Fig. 4(a). To compare with experiment, the width of the momentum distribution σ_{pz} and chirp parameter a are varied to fit the trajectory $\sigma_z(t)$ (see Fig. 2(a)). We find that the initial pulse length $\sigma_z(t=0)$, which is expected to be in the sub-micron range, has limited

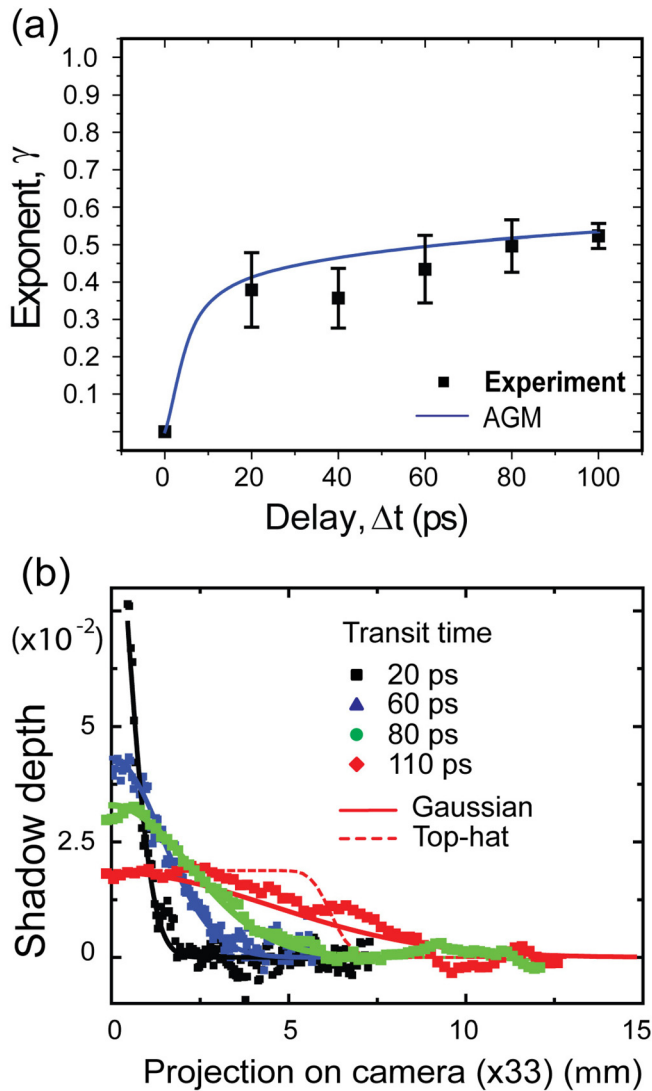


FIG. 3. (Color online) (a) The symbols represent the values of γ found at different delay times. The solid line represents results from an analytical Gaussian model (AGM) simulation using broadened initial longitudinal velocity spread due to near cathode space charge effect extracted by fitting the early time σ_z trajectory, which is presented in Fig. 4(c) and the text. (b) The symbols are the linescans of the shadow images recorded on the phosphor/CCD screen produced by photoelectrons ($\Sigma = 7.12 \times 10^{13} \text{ e/m}^2$) at different times. The linescans are fitted with a Gaussian profile (solid lines). A top-hat profile (dashed line), convoluted with the projection geometry, is also drawn for comparison. The magnification of the projection imaging is ≈ 33 .

influence on the results of the simulations at later times ($t > 10$ ps), as the pulse length expands to μm scale within a few ps. Simulations have been performed at $\sigma_z(t=0) = 30 \text{ nm}$, $1 \mu\text{m}$, and $2 \mu\text{m}$ to confirm this. Thus $\sigma_z(t=0)$ is set to the resolution limit ($1 \mu\text{m}$) of the experiment to remove this as an adjustable parameter in comparing with experimental data. At a given σ_{pz} , we find that $a=0$ gives the minimum σ_z , while $a=1$ gives the highest σ_z , as shown in Fig. 4(b). This sensitivity to the initial conditions allows us to parameterize the initial photoelectron phase space. The fitting results based on this parameterized N-particle simulation show a strong growth of the initial velocity spread obtained by $\Delta v_z(t=0) = \sigma_{pz}/m_e$ as the charge density Σ

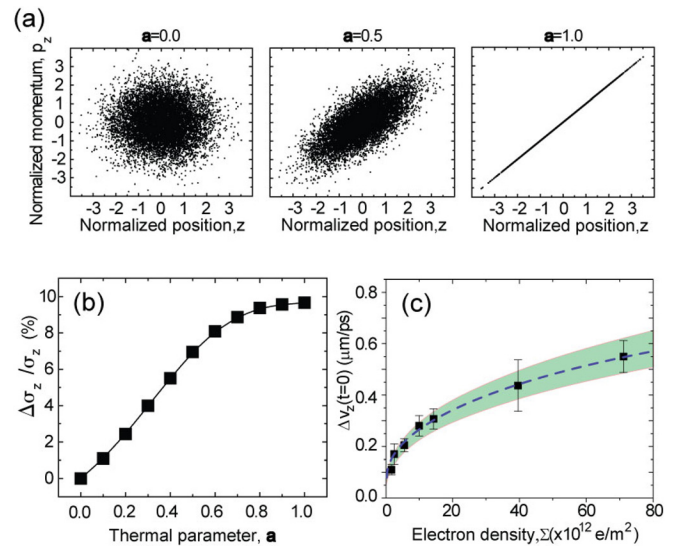


FIG. 4. (Color online) (a) The normalized “initial” longitudinal phase space employed in the N-particle simulations, which is parameterized by a thermal parameter a and scaled by the initial length σ_{zi} and momentum spread σ_{pz} . (b) The percentage change in the pulse length σ_z obtained at 100 ps as a function of a . (c) The initial longitudinal velocity spread, $\Delta v_z(t=0)$, obtained by fitting N-particle trajectories to the imaging data depicted in Fig. 2(a). The extraction field F_a applied is 0 at the five lowest Σ s, 0.32 MV/m at $40 \times 10^{12} \text{ e/m}^2$ and at $70 \times 10^{12} \text{ e/m}^2$.

increases, as indicated in Fig. 4(c). The observed significant increase of initial velocity spread of electron pulse generation can be associated with a near cathode space charge effect at the ultrashort time scale, modifying the electron energy distribution from the single-electron emission regime. In contrast, the low density photoelectron velocity spread at $\Sigma \approx 0$ can be extrapolated from results in Fig. 4(c), and thus determined $\Delta v_z(t=0) = 0.084 \pm 0.019 \mu\text{m/ps}$ represents the intrinsic, unperturbed initial velocity spread from photoemission. We note that the rapid increase of $\Delta v_z(t=0)$ cannot have come from the reduced effective work function due to applied F_a (Schottky effect). In fact, for the lowest five Σ s, the applied field is the same ($F_a = 0$), and for the highest Σ , the corresponding energy spread approaches 1 eV. Moreover, for all simulations, the strong thermal parameter range $a=0.0-0.4$ gives a better fit to the data than the correlated limit, $a=1$, inducing a near stochastic initial photoelectron distribution.

Even though mean field theory cannot fully characterize the observed early time pulse dynamics, we are able to reproduce the N-particle results presented in Fig. 2(a) using the analytic Gaussian model (AGM) developed by Michalik and Sipe^{33,34} with the initial conditions according to those refined by N-particle fitting (Fig. 4(c)). This is warranted as, within the observed time scale, the pulse profile resembles a Gaussian (Fig. 3(b)); thus, the associated pulse spreading due to nonlinear space-charge force can be properly modeled by AGM. In the following, we substitute the N-particle simulation with the less computationally expensive AGM to investigate the cause of the scaling behavior identified in the space-charge-led pulse spreading with various initial conditions. Figure 5 shows the comparison of AGM and the experimental results. The solid lines show the AGM simulations

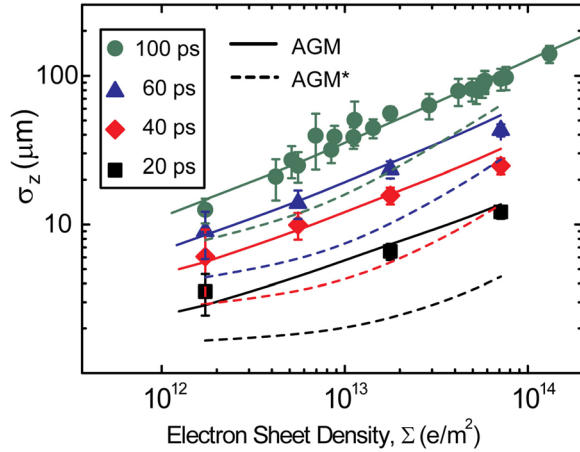


FIG. 5. (Color online) The symbols represent the experimental longitudinal pulse length (σ_z) of the photoelectron pulses with different densities tracked at different times. The solid line represents the analytical Gaussian model simulation using the different initial longitudinal velocity spread specified by Fig. 4(c) and the initial slope of phase space set to 0. The dotted line represents the analytical Gaussian model simulation using a constant initial longitudinal velocity spread $\Delta v_z(\Delta t = 0) = 0.084 \mu\text{m}/\text{ps}$.

with the initial conditions given by the N-particle refinement, which correctly predict the trends of the experimental results. In particular, the increase of σ_z over Σ bears a resemblance to the power-law, with an exponent γ increasing from 0 to near 0.5 (Fig. 3(a), solid line). In contrast, with a constant initial velocity spread of $0.084 \mu\text{m}/\text{ps}$ (the single-electron limit), while also showing incremental increase of slope, AGM* results severely underestimate $\sigma_z(\Sigma)$, as shown in Fig. 5. The compliance of N-particle simulation and AGM with our experimental results indicates that the initial electron velocity spread is crucial for the transient power-law behavior observed experimentally. As to the cause of the initial velocity spread, we attribute it to the near-cathode space charge effect. Note that the space-charge-induced energy spread has previously been studied for photoemission experiments.^{35,36,38} These studies mainly investigate the long time limit of space-charge effect that is different from the short time behavior, which embodies near-cathode space charge effect. The robust trend of $\Delta v_z(\Delta t = 0)$ as a function of electron density in Fig. 4(c), obtained using a range of F_a and F , shows that neither laser heating (F effect) nor Schottky effect (F_a effect) is the main cause of photoelectrons gaining initial velocity spread, indicating primarily a space charge effect in its origin.

C. Three step model of photoemission

To further understand the near-cathode space charge effect in the generation of photoelectrons it is instructive to compare the observed photoelectron dynamics at $\Sigma = 0$ limit with Spicer's three step model (TSM),³⁷ which has been further elucidated recently by Jensen^{30,31,40} and Dowell³⁹ to model experimental results primarily for the development of free electron lasers. In TSM, which is designed to treat photoemission at the single-electron limit, photoexcitation gives a constant energy boost $\hbar\omega$ to electrons, while maintaining a thermal energy spread based on the initial Fermi-Dirac (FD)

distribution, as shown in Fig. 6(a) (note FD width is exaggerated here for illustration purpose). To overcome the effective surface work function Φ_{eff} , particle selection is made based on a cut in momentum space at p_z^0 , which gives $\theta_{\text{max}}(E) = \cos^{-1} \sqrt{(E_F + \Phi_{\text{eff}})/(E + \hbar\omega)}$, as depicted in Fig. 6(b). Here, E is the total energy of the electron before photon absorption, with $\Phi_{\text{eff}} = \Phi_w + \Phi_{\text{Sch}}$, where $\Phi_{\text{Sch}} = e \sqrt{eF_a/4\pi\epsilon_0}$ is the Schottky value.³⁹ The electron velocity distribution following photo-absorption can be modeled by $v_z^{\text{in}} = \sqrt{2(E + \hbar\omega)/m_e} \cdot \cos(\theta)$, whose distribution is calculated using FD statistics and the momentum cut model. The shaded area marks those electrons with sufficient energy to escape the cathode surface in the absence of electronic thermalization. Here, θ is the internal emission angle approaching the surface, which falls in the range $[0, \theta_{\text{max}}]$, as depicted in Fig. 6(b). The external velocity distribution can then be calculated from v_z^{in} by considering the interface refraction: $v_z^{\text{out}} = \sqrt{2 \times [m_e(v_z^{\text{in}})^2/2 - E_F - \Phi_{\text{eff}}]}/m_e$. We want to note that TSM has been employed successfully to estimate the thermal emittance for metallic photocathodes to within a factor of 2 agreement with the experimentally determined values.^{30,39}

To provide a self-consistent, near-cathode space charge model, we first determine the work function Φ_w of our gold cathode by comparing the measured initial velocity spread $\Delta v_z(\Delta t = 0)$ extrapolated to the single-electron limit ($\Sigma = 0$) with the TSM prediction. We use both N-particle simulation and the TSM analytical model (Eq. (34) in Ref. 39) to establish the relationship between $\Delta v_z(\Delta t = 0)$ and Φ_w , as shown in Fig. 7(a). The agreements are generally good, with small deviations mainly in the low ϕ_w regime, which are sampling errors due to finite number of electrons (10^4) used in the N-particle simulation. We find that convoluting the 0.03 eV bandwidth of the 50 fs laser pulse to model the initial phase

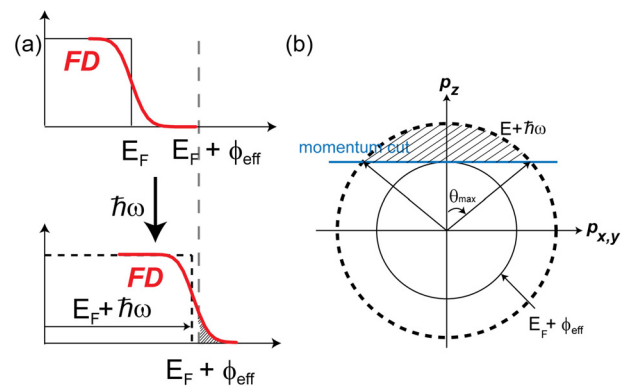


FIG. 6. (Color online) Momentum cut model for selecting electrons for photoemission used in the three step model. (a) The electron energy distribution before and after photoexcitation. In this model, the electrons are assumed to escape the cathode surface before thermalization and thus have the same Fermi-Dirac (FD) energy spread (exaggerated for illustration purpose) defined at the temperature prior to photoemission. The shaded area ($E \geq E_F + \Phi_{\text{eff}}$) represents the electron population that is qualified for photoemission. (b) The selection of electrons in the three-dimensional momentum phase space that are qualified for photoemission. The electron must have an energy larger than $E_F + \Phi_{\text{eff}}$, as described in (a); it must also have a minimum longitudinal momentum (p_z^0) to overcome the work function in order to escape the surface, as specified by the shaded area.

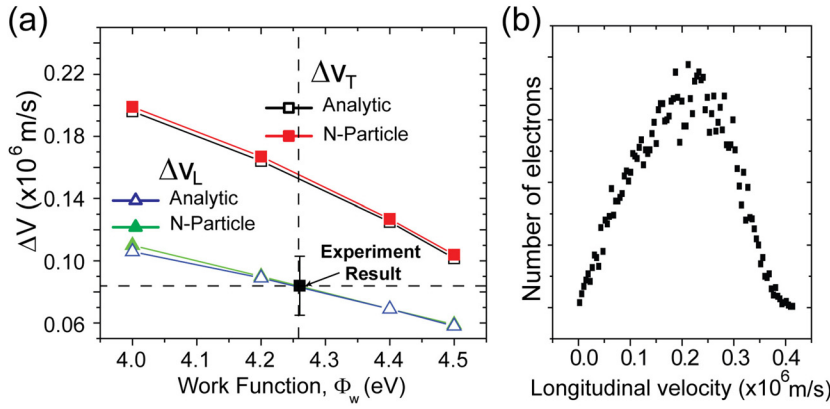


FIG. 7. (Color online) (a) The photoelectron velocity spread in the longitudinal (Δv_L) and transverse (Δv_T) directions. The solid symbols represent results obtained using N-particle simulation, and the hollow symbols represents results obtained by integrating the analytical equation reported in Ref. 39. (b) The longitudinal velocity distribution of photoelectrons generated by N-particle simulation based on the three step model.

space of photoelectrons does not significantly alter the result. Based on $\Delta v_z(\Delta t = 0) = 0.084 \pm 0.019$ $\mu\text{m}/\text{ps}$, we deduce work function $\Phi_w = 4.26 \pm 0.16$ eV for the gold photocathode, which is consistent with literature values.^{24,25} We note that the initial velocity distribution predicted by the TSM is anisotropic, as the longitudinal velocity spread is roughly a factor of two smaller than the transverse velocity spread. This can be understood with the momentum cut model in selecting the electrons for photoemission, as shown in Fig. 6, where the extent of the eligible momentum phase space for photoemission along the transverse direction (p_{xy}) is larger than that along the direction perpendicular to the surface (p_z). The N-particle simulation validated here is further employed to model the photoelectron dynamics near the surface to understand the near cathode space charge effect on the photoemission quantum yield.

D. Space-charge limitation of pulsed photoemission quantum yield

The strong image charge potential associated with the fs electron bunch, which is a thin disk during this period, modifies the surface Schottky potential Φ_{Sch} for field-assisted emission, as illustrated in Fig. 8(a). This phenomenon explains why our experimentally determined field-assisted quantum efficiency (QE), as depicted in Fig. 8(b), is much smaller than the single-electron TSM limit,³⁹ which can be calculated following Eq. (3) in Ref. 39 using F and F_a employed in our experiment. Here, QE is defined as $\text{QE} = \Sigma / (F/\hbar\omega)$, where F is the incident laser fluence. The single-electron QE thus obtained is $\approx 3.0 \times 10^{-5}$ (based on $F = 5.0$ mJ/cm^2 , the reflection coefficient $R = 0.36$, the laser absorption depth $\lambda_{opt} = 9.5$ nm,⁴¹ and the mean free path of the photo-excited electrons $\lambda_{e-e} = 6.5$ nm³⁷) and depends strongly on Φ_w , but weakly on F_a . To estimate the repulsive dipole potential Φ_{dp} associated with image charges, we use an N-particle disk model with an initial velocity distribution calculated based on the TSM, as shown in Fig. 7(b). The electron pulse is divided into 5000 slices, leading to a set of 5000 discs of transverse radius $R = 100$ μm . Due to the pairwise repulsive forces between the slices, some electron slices return to the photocathode, so we obtain R_{esp} , which is defined as the ratio of the forward moving electrons relative to the total electrons emitted. In the inset to Fig. 8(b), we plot the results obtained for $\Phi_w = 4.26$ eV, showing that R_{esp} drops significantly in the first 20 fs, indicating a rapid

return of electrons to the surface. Multiplying the transient R_{esp} , evaluated at 5 ps, by the TSM QE yields a space-charge-limited QE in semi-quantitative agreement with experiment.

While the QE can be improved by increasing the applied excitation photon flux or reducing Φ_w and/or increasing $\hbar\omega$ to expand the available phase space for photoemission, nonetheless, a fundamental space charge limitation arises when the surface dipole field associated with emitted electrons exceeds the extraction field, as has been described by an analytical virtual cathode model.⁴² The virtual cathode emission threshold is determined by treating the emitted electrons as a sheet of charge density Σ , which reduces the field at the surface of the cathode according to $F_s = F_a - \Sigma/\epsilon_0$. Photoemission ceases when the applied field F_a is completely screened ($F_s = 0$), leading to a pulse-length independent emission threshold $\Sigma_C = \epsilon_0 F_a$, a threshold that depends linearly on the extraction field. This simple model predicts a threshold $\Sigma_C = 1.77 \times 10^{13}$ e/m^2 at $F_a = 0.32$ MV/m. The analytical virtual cathode model is tested by our experiment in the fs photoemission regime. We find a saturation of photoelectron flux appears nominally at $\Sigma = 7 \times 10^{13}$ e/m^2 according to Fig. 8(c), which is nearly four times larger than the predicted threshold. The discrepancy may be attributed to the approximations inherent in the virtual cathode screening field and to the initial velocity effects that yield photoemission even when $F_a = 0$, as shown in the inset of Fig. 8(c). Nevertheless discrepancies remain, and a more sophisticated N-particle photoemission model is required to replace the analytical approach to fully account for the virtual cathode effect in the fs regime.

E. The effect of multi-photon photoemission

It is prudent to examine whether or not the near-cathode energy spread might be affected by multi-photon photoemission expected from fs photoexcitation. From the photoemission quantum efficiency study shown in Fig. 8(c), which is sub-linear with respect to fluence, we might conclude that the multi-photon photoemission is not yet prominent in the fluence regime investigated here. If the multi-photon photoemission is important, the initial energy spread will significantly increase due to the generally much larger excess energy associated with multi-photon photoionization ($\Delta E = n\hbar\omega \geq 5$ eV). From the data presented in Figs. 2(b) and 4(c), we have not seen an explicit fluence dependence,

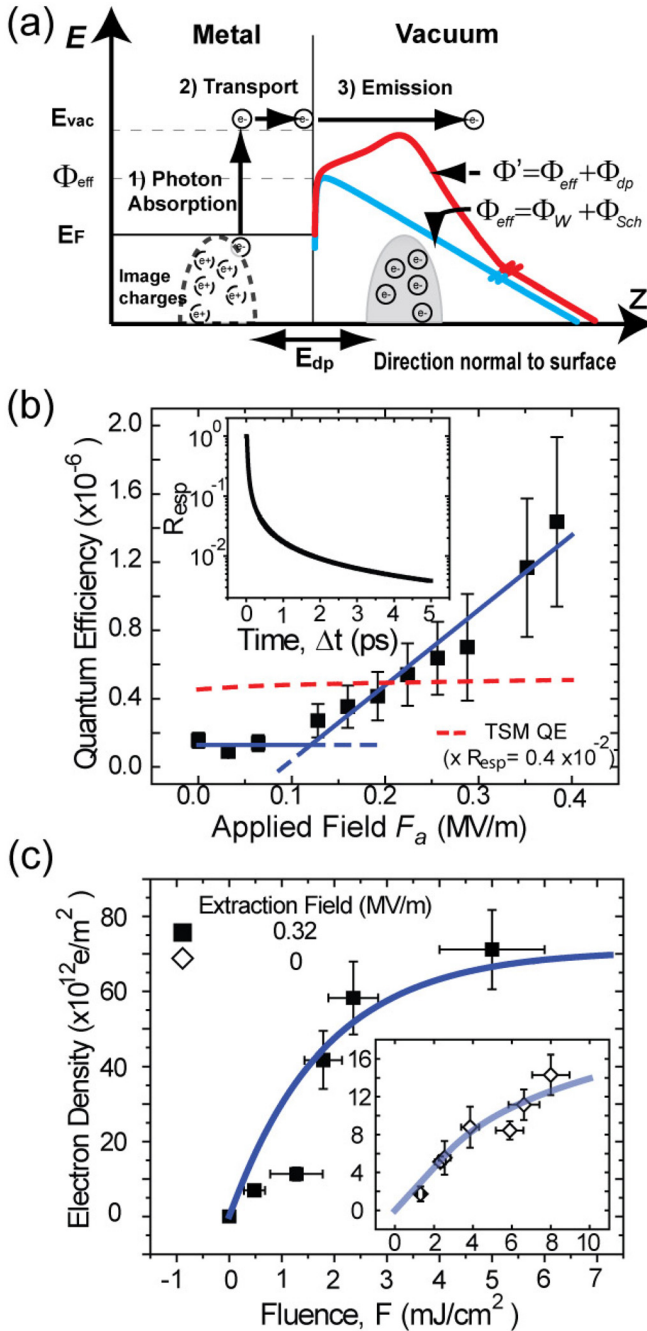


FIG. 8. (Color online) (a) Schematic of an extended three step model for intense photoemission. The net work function Φ' is the sum of the Schottky potential Φ_{Sch} , the surface dipole potential Φ_{dp} , and the intrinsic work function Φ_w . (b) The quantum efficiency derived based on modified TSM (dashed line) for $\Phi_w = 4.26$ eV and the experimental data with a fit to a constant behavior at low field and a linear behavior at high field. (Inset) The electron escape ratio, R_{esp} , is calculated, including the dipole field of the virtual cathode and its image for $\Phi_w = 4.26$ eV. (c) Electron pulse sheet density as a function of fluence for high applied field and for zero applied field (inset).

which seems to further confirm that the multi-photon ionization is a much less effective channel. Nonetheless, we cannot completely rule out its contribution, albeit being a minor channel, in increasing the initial energy spread through thermalization with the low energy electrons from the single-photon channel. Such an issue is best investigated in a

multi-photon photogun configuration, where the photoemission is driven using laser pulse with energy less than the work function of the cathode, where only multi-photon ionization contributes to the photoemission in the future.

IV. SPACE AND TIME RESOLUTIONS IN ULTRAFAST ELECTRON DIFFRACTION AND IMAGING SYSTEMS

We have shown, from our ultrafast imaging of electron pulse generation, the important role of the near-cathode space charge effect in modifying initial phase space of the photoelectrons, which dictates the ensuing space charge dynamics. The energy spreading associated with such an effect easily exceeds the intrinsic electron energy spread predicted by the three step model (TSM). This energy spread is different from a Coulomb-explosion-led one, as the near cathode space charge effect increases the thermal emittance, whereas the energy spreading due to the Coulomb explosion is largely manifested through momentum chirping, not necessarily leading to emittance growth.^{43,44} This recognition is important in addressing the space charge effects in the development of a high-brightness electron beam system for the next generation ultrafast electron diffraction (UED) and microscopy (UEM). According to the studies presented here, the fundamental limitations for the temporal resolution and beam brightness would not completely lie in the free space Coulomb explosion effect, which, albeit being the main contributor for degrading the time resolution in the current UED systems, could be largely corrected using an RF pulse recompression scheme.

The effectiveness of RF recompression^{11,14,17,18} to eliminate the free space Coulomb explosion effect can be shown with the N-particle beam dynamics simulation in an electron optical column incorporating an RF cavity, as depicted in Fig. 9. While the random pairwise Coulomb interactions within the electron pulse cause some spill-offs in the chirped phase space, the majority of the longitudinal phase space occupied by photoelectron prior to the RF cavity is linear, as shown in Fig. 9(a). RF field can reverse the chirping to achieve a temporal refocusing and in the subsequent sample plane, where the chirp axis becomes vertical to z . We observed that, similar to transverse focusing characteristics, choosing a short focal length leads to a higher recompression ratio at an expense of larger spreading in p_z . Recently, such a recompression scheme has been successfully implemented to produce an intense ($\approx 10^6$ electrons) femtosecond electron pulse, achieving a recompression ratio better than 100 (from 10 ps to ≈ 100 fs)⁴⁵ without significant lateral compression. The ultimate limitation for high-brightness beam generation thus lies in the emittance growth by the near-cathode space charge effect and the virtual cathode limitation in photoelectron quantum efficiency. Whereas the virtual cathode limitation can be partially alleviated by employing a high extraction field up to the breakdown limit (practical breakdown limit: DC gun ≈ 8 MV/m, RF gun ≈ 30 MV/m, and ≥ 100 MV/m for superconducting RF gun), the initial emittance growth inherent at a high charge density, desired for a high-brightness beam, will likely remain an issue for achieving high spatial and temporal resolutions in UED and UEM.

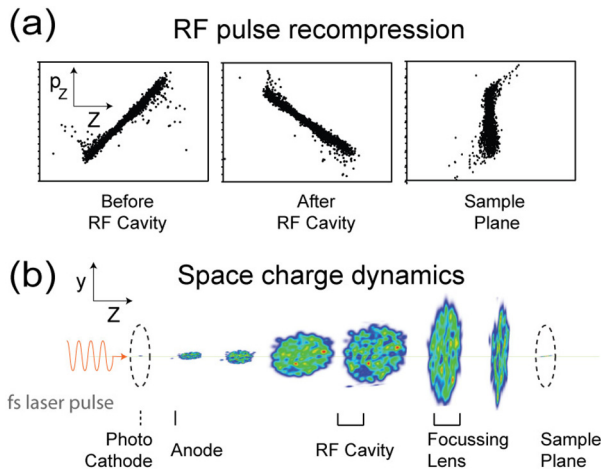


FIG. 9. (Color online) Concept of an electron beam injector column for ultrafast electron microscope demonstrated using an N-particle simulation of electron pulse propagation in an electron beam column with an RF cavity. (a) Phase space adjustment before and after the RF cavity. (b) The corresponding real space pulse profile at each electron optical components. The simulation is performed using 10^4 electrons per pulse at 30 keV using the initial condition $a = 1$, as specified in Fig. 4(a).

To evaluate this fundamental limit, we conduct calibrated analytical Gaussian model (AGM)^{33,34} calculations as described earlier using initial conditions defined according to the near-cathode space charge effect elucidated here. We note that the results from AGM calculation represent the ideal cases for beam optimization as AGM conserves the beam emittance, which means that the only limitation for achieving optimal spatial and temporal focusing in a UEM column is the initial beam emittance and the RF and electron optical arrangement for space and time focusing. We first simulate the temporal resolutions of UED and UEM without incorporating RF compression and show in Fig. 10(a) that the simulations (symbols) are consistent with the reported ranges of temporal resolution in UED^{1,2,6,27} and UEM^{5,8} systems, which are shown as rectangular shaded areas, for the respective N_e per pulse. The difference in time resolution between UEM (solid squares) and UED (hollow diamonds) comes from the flight distance chosen here (for UEM, the cathode-to-sample distance is 70 cm; for UED, it is 5 cm) and different beam energy (for UEM, the beam energy is 100 keV; for UED, it is 30 keV). For low flux applications, single-electron UEM systems eliminate the space charge effects by incorporating a high-repetition rate (at 100 MHz level) fs laser trigger; thereby, fs time resolution and high coherence length can be achieved.⁵ Nonetheless, the time resolution calculated for single-electron UED and UEM is fundamentally limited by the shot-to-shot temporal fluctuation of the photoelectrons, determined by their intrinsic thermal velocity spread.^{25,30} In comparison, we evaluate for high brightness beam generation, under the idealized AGM scheme, the best scenario for improving the temporal resolution. We consider an electron beam column consisting of a 100 keV DC gun, two pre-compressor magnetic lenses, an RF compressor, an aperture, and a short-focal-distance (< 1 cm) objective lens, as described in

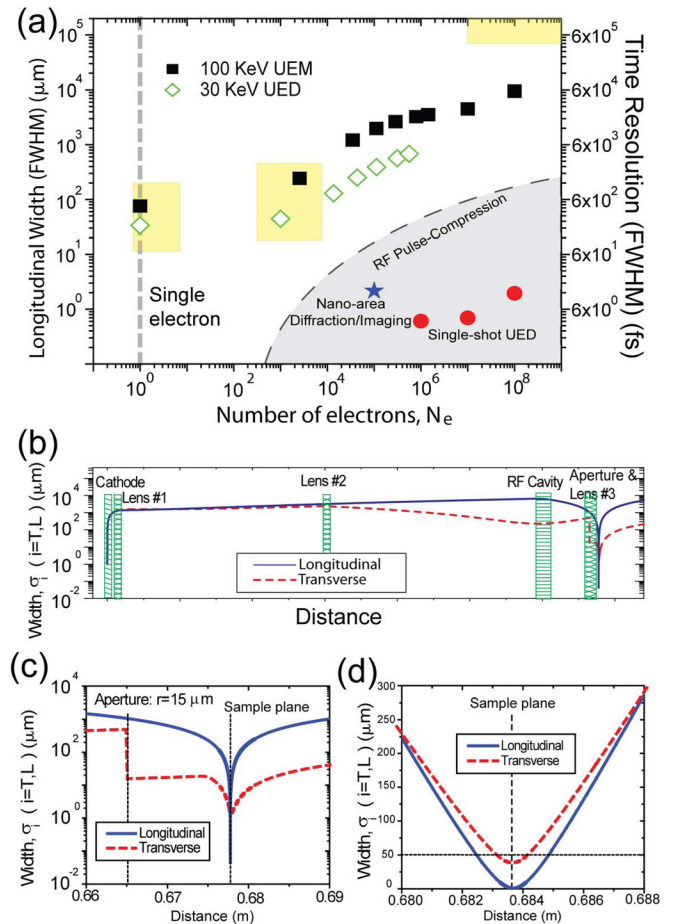


FIG. 10. (Color online) (a) Space-charge-limited temporal resolutions in ultrafast electron diffraction (UED) and microscopy (UEM) systems. Solid squares and hollow diamonds show the Coulomb-explosion-led pulse lengthening calculated for 100 keV UEM system (squares) with cathode-to-sample distance of 70 cm and 30 keV UED system (diamonds) with cathode-to-sample distance of 5 cm. The rectangular shaded areas depict experimental resolutions reported in current UED and UEM systems. In comparison, the solid stars and circles show the improvements in temporal resolution by employing an RF recompression in the UEM beam column (see panel (b)) optimized for nano-area diffractive imaging (stars) and for single-shot UED (circles). (b) Photoelectron pulse trajectory along an RF-enabled UEM column. The shaded regions represent the locations of the electron optical elements. (c) A scale-up view of the pulse profiles near the sample plane for nano-area diffractive imaging containing 10^5 electrons/pulse. An aperture with radius of $15 \mu\text{m}$ is employed to thin out the peripheral electrons to achieve a divergence angle $\alpha \leq 1.7$ mrad. The minimum transverse radius σ_T is $0.64 \mu\text{m}$, and the minimum longitudinal pulse length σ_L is $0.80 \mu\text{m}$. (d) A scale-up view of the pulse profiles near the sample plane for an ultrafast single-shot UED containing 10^8 electrons/pulse. The minimum transverse radius σ_T is $51 \mu\text{m}$, and the minimum longitudinal pulse length σ_L is $0.88 \mu\text{m}$.

Fig. 10(b) and Table I. The optimization of the beam quality delivered to the sample plane depends largely on overcoming the strong interplay between the longitudinal and transverse degrees of freedom due to the space charge effect. The strong transverse defocussing induced by intense space charge force near the focal plane due to longitudinal focusing is compensated by higher strength of the magnetic lens to reach simultaneous focusing (longitudinal and transverse). Specifically here, we consider two regimes of operation. First, for nano-area diffractive imaging,⁴⁶ the corresponding beam parameter requirements are the transverse coherence length $L_T \geq 1$ nm

TABLE I. Location of electron optical components in the UEM column.

| Electron optical component | Position (m) |
|----------------------------|--------------|
| Cathode | 0 |
| Anode | 0.0125 |
| Magnetic lens #1 | 0.020 |
| Magnetic lens #2 | 0.300 |
| RF cavity | 0.600 |
| Aperture | 0.665 |
| Magnetic lens #3 | 0.675 |

and the electron probe size $\sigma_T \leq 500$ nm. Such beam characteristics will also be applicable for UEM.^{2,5,18} Second, for single-shot ultrafast electron diffraction, we maintain the coherence length $L_T \geq 1$ nm while the requirement of $\sigma_T \leq 500$ nm is relaxed, thereby allowing higher electron intensity ($\geq 10^6$ electrons per pulse). Such beam characteristics are suited for studying the irreversible process.^{6,22} An optimization to simultaneously achieve high lateral coherence L_T (≥ 1 nm) (L_T is calculated according to $L_T = \lambda_e/2\alpha$, where $\lambda_e = 0.0037$ nm is the electron wavelength and α is the half divergence angle at the sample plane determined based on $\alpha = \Delta v_T/v_e$, where $v_e = 1.64 \times 10^8$ m/sec is the relativistic electron CoM velocity at 100 keV. To allow for $L_T \geq 1$ nm, the beam's half divergence angle at the sample plane must satisfy $\alpha \leq 2$ mrad.) and spatial resolution (lateral probe size) σ_T (≤ 500 nm) for UEM is demonstrated in Fig. 10(c). Under this tight simultaneous spatial and temporal focusing requirement, achieved by a small aperture in front of the objective lens to maintain a long coherence length, the available photoelectrons is reduced to 10^5 electrons per pulse. On the other hand, if the lateral confinement is not required, the beam emittance can be significantly increased under the same constraints for maintaining the fs pulse length and high lateral coherence (at the expense of increasing the lateral size), and so up to 10^8 electrons per pulse can be obtained for single-shot diffraction, as shown in Fig. 10(d). We note the AGM calculation conducted here incorporates the external field extension⁴⁷ developed by Berger and Schroeder to model the magnetic lenses and the RF cavity. We also consider the acceleration gap effect, which arises from the difference in travel time for photoelectrons due to different initial velocity and space charge effects, leading to an adjustment of momentum distribution of the pulse crossing the acceleration gap,

$$\delta p_z = \frac{\gamma_c m_e c}{2} \left(\sqrt{1 - \left(\frac{1}{\gamma_c + \Delta v_z^2/2c^2} \right)^2} - \sqrt{1 - \left(\frac{1}{\gamma_c - \Delta v_z^2/2c^2} \right)^2} \right), \quad \text{where } \gamma_c = \frac{1}{\sqrt{1 - v_e^2/c^2}},$$

v_e is the electron bunch COM velocity, and Δv_z is the longitudinal velocity deviation at the anode.

While the AGM model provides a rather promising outlook for the development of an RF-enabled high-brightness UEM, the technical challenges to achieve the prescribed spatial and temporal resolutions, as outlined in Fig. 10(a), cannot be under-estimated. The parameters for achieving the space-time focusing will likely vary from the optimization provided by AGM when considering the inhomogeneous electron bunch, which would develop in a realistic beam sys-

tem from instabilities associated with photoemission and random pair-wise interactions between electrons (as shown in Fig. 9) and the nonlinear effects in the RF cavity and the aberration associated with electron optics. Clocking the RF field with fs laser pulse to the precision demanded by the required temporal resolution is needed. Fortunately, these technologies do exist in the mature fields of electron microscopy⁴⁸ and precision RF-laser synchronization⁴⁹ and can be incorporated in the development of RF-enabled UEM. An efficient multilevel fast multipole approach⁵⁰ recently developed to account for arbitrary shape pulse dynamics for RF-UEM development has shown a great promise to effectively model the high intensity UEM beam at $\geq 10^8$ e/pulse level with explicit details of the nonlinear effects. In particular, the ultrafast shadow imaging probe can be applied to different cathode designs and be incorporated at different stages (before and after the RF cavity) along the column to characterize the transient beam characteristics. Different from other ultrashort pulse characterization methods,^{1,51,52} the imaging probe provides simultaneous full-scale longitudinal and transverse pulse characterization, which is ideally suited to directly compare with beam dynamics simulations, thus forming an experimentally informed optimization scheme in designing electron optics for future high-brightness UEM systems.

ACKNOWLEDGMENTS

We acknowledge fruitful discussions with K. Chang, K. Makino, M. Doleans, and A. M. Michalik. This work was supported by the DOE under grant DE-FG02-06ER46309 and by a seed grant for the development of a RF-enabled ultrafast electron microscope from the MSU Foundation.

- ¹R. Srinivasan, V. A. Lobastov, C.-Y. Ruan, and A. H. Zewail, *Helv. Chim. Acta* **86**, 1763 (2003).
- ²A. Gahlmann, S. T. Park, and A. H. Zewail, *Phys. Chem. Chem. Phys.* **10**, 2894 (2008).
- ³B. J. Siwick, J. R. Dwyer, R. E. Jordan, and R. J. D. Miller, *J. Appl. Phys.* **92**, 1643 (2002).
- ⁴W. E. King, G. H. Campbell, A. Frank, B. Reed, J. F. Schmerge, B. C. Stuart, and P. M. Weber, *J. Appl. Phys.* **97**, 111101 (2005).
- ⁵A. H. Zewail and J. M. Thomas, *4D Electron Microscopy: Imaging in Space and Time* (Imperial College Press, London, 2010).
- ⁶G. Sciaini, M. Harb, S. G. Kruglik, T. Payer, C. T. Hebeisen, F.-J. M. Heringdorf, M. Yamaguchi, M. H. von Hoegen, R. Ernstorfer, and R. J. D. Miller, *Nature* **458**, 56 (2009).
- ⁷R. K. Raman, R. A. Murdick, R. J. Worhatch, Y. Murooka, S. D. Mahanti, T. R. Han, and C.-Y. Ruan, *Phys. Rev. Lett.* **104**, 123401 (2010).
- ⁸J. S. Kim, T. LaGrange, B. W. Reed, M. L. Taheri, M. R. Armstrong, W. E. King, N. D. Browning, and G. H. Campbell, *Science* **321**, 1472 (2008).
- ⁹D. H. Dowell, I. Bazarov, B. Dunham, K. Harkay, C. Hernandez-Garcia, R. Legg, H. Padmore, T. Rao, J. Smedley, and W. Wan, *Nucl. Instrum. Methods Phys. Res. A* **622**, 685 (2010).
- ¹⁰S. J. Russel, *Nucl. Instrum. Methods Phys. Res. A* **507**, 304 (2003).
- ¹¹T. van Oudheusden, E. F. de Jong, S. B. van de Geer, W. P. E. M. O. Root, O. J. Luiten, and B. J. Siwick, *J. Appl. Phys.* **102**, 093501 (2007).
- ¹²P. Musumeci, J. T. Moody, C. M. Scoby, M. S. Gutierrez, and M. Westfall, *Appl. Phys. Lett.* **97**, 063502 (2010).
- ¹³B. E. Carlsten and S. J. Russell, *Phys. Rev. E* **53**, R2072 (1996).
- ¹⁴L. Veisz, G. Kurkin, K. Chernov, V. Tarnetsky, A. Apolonski, F. Krausz, and E. Fill, *New J. Phys.* **9**, 451 (2007).
- ¹⁵P. Baum and A. H. Zewail, *Proc. Natl. Acad. Sci. U. S. A.* **103**, 16105 (2006).
- ¹⁶X. J. Wang, D. Xiang, T. K. Kim, and H. Ihee, *J. Korean Phys. Soc.* **48**, 390 (2006).

- ¹⁷J. B. Hastings, F. M. Rudakov, D. H. Dowell, J. F. Schmerge, J. D. Cardoza, J. M. Castro, S. M. Gierman, H. Loos, and P. M. Weber, *Appl. Phys. Lett.* **89**, 184109 (2006).
- ¹⁸J. A. Berger, J. T. Hogan, M. J. Greco, W. A. Schroeder, A. W. Nicholls, and N. D. Browning, *Microsc. Microanal.* **15**, 298 (2009).
- ¹⁹R. K. Raman, Z. Tao, T. R. Han, and C.-Y. Ruan, *Appl. Phys. Lett.* **96**, 059901 (2010).
- ²⁰A. Janzen, B. Krenzer, O. Heinz, P. Zhou, D. Thien, A. Hanisch, F. J. Meyer zu Heringdorf, D. von der Linde, and M. Horn von Hoegen, *Rev. Sci. Instrum.* **78**, 013906 (2007).
- ²¹L. A. Lobastov, R. Srinivasan, and A. H. Zewail, *Proc. Natl. Acad. Sci. U. S. A.* **102**, 7069 (2005).
- ²²T. LaGrange, M. R. Armstrong, K. Boyden, C. G. Brown, G. H. Campbell, J. D. Colvin, W. J. DeHope, A. M. Frank, D. J. Gibson, F. V. Hartemann, J. S. Kim, W. E. King, B. J. Pyke, B. W. Reed, M. D. Shirk, R. M. Shuttlesworth, B. C. Stuart, B. R. Torrala, and N. D. Browning, *Appl. Phys. Lett.* **89**, 044105 (2006).
- ²³T. Srinivasan-Rao, J. Fischer, and T. Tsang, *J. Appl. Phys.* **69**, 3291 (1990).
- ²⁴X. Jiang, C. N. Berglund, A. E. Bell, and W. A. Mackie, *J. Vac. Sci. Technol. B* **16**, 3374 (1998).
- ²⁵M. Aidelsburger, F. O. Kirchner, F. Krausz, and P. Baum, *Proc. Natl. Acad. Sci. U. S. A.* **107**, 19714 (2010).
- ²⁶L. M. Rangarajan and G. K. Bhide, *Vacuum* **30**, 515 (1980).
- ²⁷C.-Y. Ruan, Y. Murooka, R. K. Raman, R. A. Murdick, R. J. Worhatch, and A. Pell, *Microsc. Microanal.* **15**, 323 (2009).
- ²⁸K. Chang, R. A. Murdick, Z. Tao, T.-R. T. Han, and C.-Y. Ruan, *Mod. Phys. Lett. B* **25**, 2099 (2011).
- ²⁹B.-L. Qian and H. E. Elsayed-Ali, *J. Appl. Phys.* **91**, 462 (2002).
- ³⁰K. L. Jensen, P. G. O'Shea, D. W. Feldman, and N. A. Woody, *Appl. Phys. Lett.* **89**, 224103 (2006).
- ³¹K. L. Jensen, P. G. O'Shea, D. W. Feldman, and J. L. Shaw, *J. Appl. Phys.* **107**, 014903 (2010).
- ³²B. W. Reed, *J. Appl. Phys.* **100**, 034916 (2006).
- ³³A. M. Michalik and J. E. Sipe, *J. Appl. Phys.* **99**, 054908 (2006).
- ³⁴A. M. Michalik and J. E. Sipe, *J. Appl. Phys.* **105**, 084913 (2009).
- ³⁵S. Hellmann, K. Rossnagel, M. Marczyński-Buhlow, and L. Kipp, *Phys. Rev. B* **79**, 035402 (2009).
- ³⁶X. J. Zhou, B. Wannberg, W. L. Yang, V. Brouet, Z. Sun, J. F. Douglas, D. Dessau, Z. Hussain, and Z. X. Shen, *J. Electron Spectrosc. Relat. Phenom.* **142**, 27 (2005).
- ³⁷W. F. Krolikowski and W. E. Spicer, *Phys. Rev. B* **1**, 478 (1970).
- ³⁸S. Passlack, S. Mathias, O. Andreyev, D. Mittnacht, M. Aeschlimann, and M. Bauer, *J. Appl. Phys.* **100**, 024912 (2006).
- ³⁹D. H. Dowell and J. F. Schmerge, *Phys. Rev. ST Accel. Beams* **12**, 074201 (2009).
- ⁴⁰K. L. Jensen, D. W. Feldman, N. A. Woody, and P. G. O'Shea, *J. Appl. Phys.* **99**, 124905 (2006).
- ⁴¹D. R. Lide, *CRC Handbook of Chemistry and Physics*, 74th ed. (CRC, Boca Raton, FL, 1993).
- ⁴²A. Valfells, D. W. Feldman, M. Virgo, P. G. O'Shea, and Y. Y. Lau, *Phys. Plasmas* **9**, 2377 (2002).
- ⁴³P. Musumeci, J. T. Moody, R. J. England, J. B. Rosenzweig, and T. Tran, *Phys. Rev. Lett.* **100**, 244801 (2008).
- ⁴⁴O. J. Luiten, S. B. van der Geer, M. J. de Loos, F. B. Kiewiet, and M. J. van der Wiel, *Phys. Rev. Lett.* **93**, 094802 (2004).
- ⁴⁵T. van Oudheusden, P. L. E. M. Pasmans, S. B. van de Geer, M. J. de Loos, M. J. van der Wiel, and O. J. Luiten, *Phys. Rev. Lett.* **105**, 264801 (2010).
- ⁴⁶J. M. Zuo, I. Vartanyants, M. Gao, R. Zhang, and L. A. Nagahara, *Science* **300**, 1419 (2003).
- ⁴⁷J. A. Berger and W. A. Schroeder, *J. Appl. Phys.* **108**, 124905 (2010).
- ⁴⁸K. W. Urban, *Science* **321**, 506 (2008).
- ⁴⁹R. K. Shelton, L. Ma, H. C. Kapteyn, M. M. Murnane, J. L. Hall, and J. Ye, *Science* **293**, 1286 (2001).
- ⁵⁰H. Zhang and M. Berz, *Nucl. Instrum. Methods Phys. Res. A* **645**, 338 (2011).
- ⁵¹C. T. Hebeisen, G. Sciaini, M. Harb, R. Ernstorfer, T. Dartigalongue, S. G. Kruglik, and R. J. D. Miller, *Opt. Express* **16**, 3334 (2008).
- ⁵²P. Musumeci, J. T. Moody, C. M. Soby, M. S. Gutierrez, and T. Tran, *Rev. Sci. Instrum.* **80**, 013302 (2009).